Additive Manufacturing 48 (2021) 102406

Contents lists available at ScienceDirect

Additive Manufacturing

journal homepage: www.elsevier.com/locate/addma

Research Paper

Suppression and reactivation of transformation and twinning induced plasticity in laser powder bed fusion additively manufactured Ti-10V-2Fe-3Al

S.A. Mantri [b,1,*], M.S.K.K.Y. Nartu [a,b,1], S. Dasari [a,1], A. Sharma [a], P. Agrawal [a], R. Salloom [a], F. Sun [c], E. Ivanov [d], K. Cho [e], B. McWilliams [e], S.G. Srinivasan [a], N.B. Dahotre [a,b], F. Prima [c], R. Banerjee [a,b,**]

[a] Department of Materials Science and Engineering, University of North Texas, Denton, TX, 76207, USA
[b] Center for Agile and Adaptive Additive Manufacturing, University of North Texas, Denton, TX, USA
[c] PSL Research University, Chimie ParisTech, Institut de Recherche de Chimie Paris, CNRS UMR 8247, 75005 Paris, France
[d] TOSOH Inc., Grove City, OH, USA
[e] Weapons and Materials Research Directorate, US Army Research Laboratory, Aberdeen Proving Ground, MD 21005, USA

ARTICLE INFO

Keywords:
Laser powder bed fusion
Transformation induced plasticity
Beta titanium alloys
Advanced characterization

ABSTRACT

Laser powder bed fusion (LBPF) was employed to fabricate a strain-transformable β-Ti alloy, Ti-10V-2Fe-3Al (wt %). While the alloy is known to exhibit transformation induced plasticity (TRIP), the as-fabricated alloy, under tensile loading, did not show the same TRIP effects, even though it exhibits the same β + ω microstructure. The repeated heating-cooling cycles experienced during the LBPF process leads to the early stages of rejection of solute elements (Fe, V, and Al), forming isothermal omega (ω) precipitates, which were captured via detailed investigations coupling transmission electron microscopy (TEM) and three-dimensional atom probe tomography (APT). While these homogeneously distributed isothermal ω precipitates lead to a higher yield strength, the TRIP/TWIP effects within the β matrix were suppressed, leading to very low ductility and virtually no strain-hardenability. Interestingly, after a simple β-solution heat treatment followed by quenching, leading to a β + ω (athermal) microstructure, the TRIP/TWIP effects were reactivated in the same LPBF Ti-10 V-2Fe-3Al alloy. The alloy exhibited substantial recovery of tensile ductility and a very large strain hardening (tensile strength minus yield strength ~500 MPa), with a high average strain hardening rate ~15000. Such a very high strain hardening rate in case of LBPF processed Ti-10 V-2Fe-3Al, appears to arise from a rapid strain-induced transformation from β to α" at the early stages of plastic deformation, leading to a high-volume fraction of the martensitic phase, coupled with hierarchical twinning within the martensite plates.

1. Introduction

Traditionally Ti alloys have been known for their high yield strengths, but rather poor strain hardenability and uniform elongation [1,2]. This has been well-established for both α/β Ti alloys such as Ti-6Al-4V as well as metastable β alloys, such as Ti-5Al-5V-5Mo-3Cr (with an α + β microstructure) [3,4]. Recently, a number of metastable β-Ti alloys have been developed that exhibit high strain hardenability and uniform elongation attributable to deformation or strain-induced twinning or martensite formation, also referred to as twinning induced plasticity (TWIP) and/or transformation induced plasticity (TRIP), versus traditional deformation via slip [5–11]. As an example, the commercially available Ti-10V-2Fe-3Al (wt%) (hereon referred to as Ti-10–2–3) alloy falls under the category of strain transformable β-Ti alloys exhibiting TRIP/TWIP effects [12]. Invariably, these strain-transformable β-Ti alloys suffer from rather poor yield strengths. Similarly, low modulus β-Ti alloys used for biomedical applications also suffer from poor yield strengths [3,4]. Therefore, there is

* Corresponding author.
** Corresponding author at: Department of Materials Science and Engineering, University of North Texas, Denton, TX, 76207, USA.
E-mail addresses: Srinivasmantri@my.unt.edu (S.A. Mantri), Raj.Banerjee@unt.edu (R. Banerjee).
[1] Authors had equal contribution.

https://doi.org/10.1016/j.addma.2021.102406
Received 12 July 2021; Received in revised form 30 September 2021; Accepted 1 October 2021
Available online 22 October 2021

a need for the compositional and microstructural design of Ti alloys with higher yield strength while maintaining their strain-transformable attributes. The other major advantages of using β-Ti alloys is their tunable nature, wherein, the microstructure and subsequently mechanical behavior can be altered by varying the thermo-mechanical processing. By controlling the secondary precipitate phases like omega or alpha, within the parent β-matrix, including their shape, size, and morphology a wide range of mechanical properties can be achieved [4,13–15].

While metal additive manufacturing (AM) has been extensively used for processing α/β Ti alloys, such as Ti-6Al-4V, there are relatively fewer investigations on AM processing of metastable β Ti alloys which have been attracting some recent attention [16–20]. While Ti-6Al-4V is an excellent alloy for many applications, there is a need to explore new titanium alloy systems, especially β-Ti alloys, in order to exploit the unique advantages which AM offers over conventional casting techniques; such advantages include faster cooling rates and complex multiple heating/cooling cycles [21,22]. Faster cooling leads to higher solidification rates which can then be exploited to process alloys which have been traditionally difficult to cast due to segregation problems. These include a class of β-Ti alloys, more specifically systems containing β-eutectoid elements such as Fe and Cu, that lead to micro-segregation issues commonly referred to as the "beta fleck" problem [3,23]. Recent literature on this has shown that the higher cooling rates obtained via AM processing can successfully overcome this issue [19,24–26].

Conventionally processed Ti-10–2–3 alloy provides an excellent combination of deep hardenability, good strength and ductility, and fracture toughness relative to Ti-6Al-4V and has therefore been one of the most widely used β-titanium alloys in the aerospace industry [3]. There have been reports of micro-segregation due to the presence of Fe in this system, which could possibly lead to property variability. As mentioned before, the higher cooling rates accessible during AM processing is a potential solution to the problem of "beta fleck" and has been recently demonstrated [26,27]. Early work by Duerig et al. [12,28] provided the groundwork in understanding the mechanical behavior and phase transformations of conventionally processed Ti-10–2–3 alloy. The presence of orthorhombic stress induced martensite (SIM) was noted in their work, which has since been confirmed by other researchers [9,29]. More recent studies focused on understanding the various factors influencing the formation of the SIM in this alloy [30–33]. While there have been a few previous studies on AM processed Ti-10–2–3 [27,34], they are very limited in terms of addressing transformation induced plasticity. The present study on laser-based powder bed fusion (LPBF) processing of the Ti-10–2–3 alloy, focuses on the influence of the LPBF processing on the evolution of the β + ω microstructure, its attendant influence on deformation behavior, and an approach to recover the TRIP/TWIP effects and strain hardenability in the AM processed alloy via a β-solution treatment.

2. Materials and methods

2.1. Additive manufacturing

The samples were fabricated using pre-alloyed, gas atomized Ti-10V-2Fe-3Al (wt%) obtained from Tosoh SMD Inc. The average powder size for this process was between 15 and 45 μm. A powder bed fusion (PBF) system, AconityMIDI, equipped with a 1KW laser was used for printing an 18 mm* 18 mm* 18 mm cube. An island scan strategy was employed with a laser power of 150 W and scan speed of 800 mm/sec, with a hatch width of 60 μm and layer thickness of 30 μm. A continuous flow of Ar (30 lpm) was deployed into the process chamber in order to maintain the O2 level below 10 ppm.

2.2. Material characterization and mechanical testing

Following the fabrication, the sample was sectioned into two parts. One of the samples was solutionized at 900 °C/30 min and then water quenched. Phase analyses via X-ray was done using a Rigaku Ultima III X-ray diffractometer for the samples, both before and after the deformation. A FEI Nova NanoSEM, coupled with an Energy Dispersive Spectroscopy (EDS) and a Hikari Super Electron Backscattered Diffraction (EBSD) detector was used for scanning electron microscopy and composition analyses. Site-specific samples for TEM analyses were prepared using a FEI Nova NanoLab 200™ focused ion beam (FIB). Transmission electron microscopy (TEM) was carried out in a FEI Tecnai F20-FEG TEM operated at 200 kV. EM based OIM - PED was carried out using a NanoMEGAS system. The parameters were set at C2 aperture of 30 μm, spot size of around 2 nm (spot size of 8 on the FEI system), camera length of 135 mm and step size of 10 nm. The data acquired using TOPSPIN 3.0 software was analyzed by ACOM software. In addition, nanometer-scale compositional analysis of the same samples was done using a 5000XS Camera LEAP 3D atom probe tomography (APT) operated at 30 K with a pulse fraction of 20% and a detection rate of 0.5 in Laser mode.

Tensile specimens were extracted from both the as-fabricated (AF) and solutionized (β-soln) plates, perpendicular to the build direction. The tensile tests were performed under a uniaxial tension at a strain of 10^{-3}/sec. A custom built mini-tensile machine with a LVDT (linear variable displacement transformer) extensometer was employed for strain measurements. The tensile samples had a gage length of 5 mm and cross section of 1.25 mm * 1.25 mm. For each condition, a total of three specimens were strained to failure, following which fracture analyses was performed on the deformed surfaces. The details of setup of mechanical testing are presented elsewhere [35].

3. Results and discussion

3.1. Microstructure and mechanical behavior of as-fabricated Ti-10–2-3 alloy

The initial microstructures of the as-fabricated (AF) samples are shown in Fig. 1a and b, corresponding to EBSD Inverse Pole Figure (IPF) + Image Quality (IQ) and Kernel Average Misorientation (KAM) plots from in-plane sections of the samples. Sectioning has been carried out perpendicular to the build axis for these in-plane sections. The in-plane view was chosen since the mechanical testing was carried out with the tensile axis lying in-plane. Arrows indicating the tensile testing direction have also been shown in the EBSD IPF maps. The starting condition of the AF sample shows single phase β grains, which are square in shape with ~75 μm sides, in this two-dimensional view. The morphology of the grains can be attributed to the island scan strategy used during the deposition, as reported in previous studies [36,37]. While the island scan strategy has been recommended for its ability to lower the residual stresses in the system during the PBF process, the KAM maps indicate a significant amount of retained residual stresses [21,22]. Tensile mechanical testing was carried out on this condition, and the results are shown in Fig. 1(c). The AF sample showed a very high value of yield strength (YS), ~850 MPa, but virtually no ductility. It should be noted that three tensile samples were tested, and Fig. 1(c) shows a representative engineering stress-strain plot. Following the tensile testing, the surface of the tensile samples clearly exhibited slip lines corresponding to very limited plastic deformation, as revealed by SEM images (Fig. 1 (d)). There was no indication of stress induced martensite (SIM, α") [38,39] formation in the deformed AF Ti-10–2–3 samples, based on these SEM images. This observation appeared to be unusual since Ti-10–2–3 with a single β phase is expected to exhibit stress-induced martensitic transformation and TRIP effects, based on multiple previous reports on conventionally processed alloys [12,28,30]. Therefore, in order to understand the deformation behavior and the lack of formation of SIM in AF Ti-10–2–3, further analysis of this sample was carried out via both TEM and Atom Probe Tomography (APT).

Fig. 2(a) shows the dark field TEM (dark-field) image of the sample

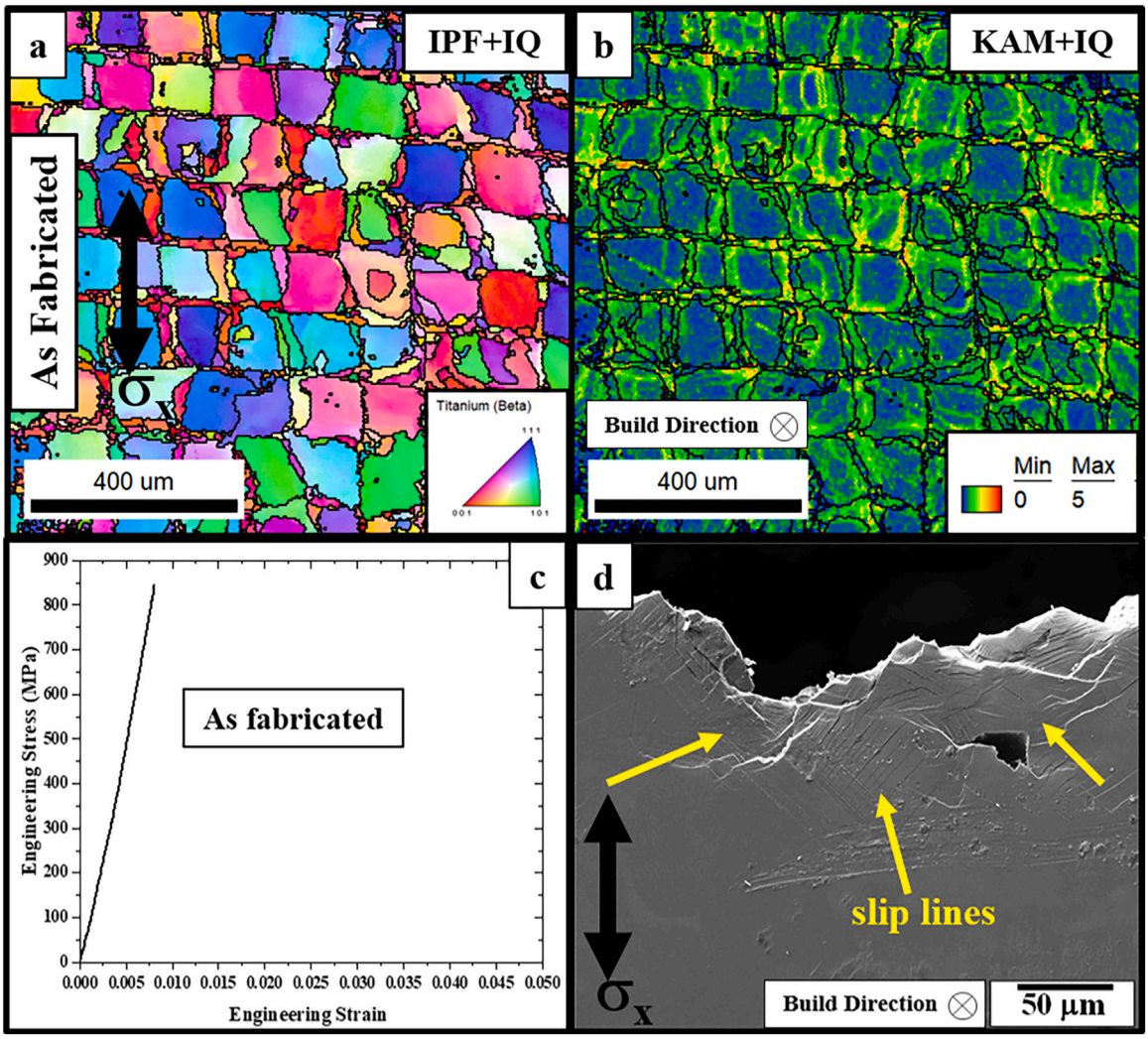

Fig. 1. Starting microstructures of the As-fabricated sample shown via EBSD IPF (a) and KAM maps (b), (c) Engineering stress vs engineering plastic strain plot of the AF sample, (d) deformed surface of the AF sample showing slip lines.

obtained from the grip section of one of the tensile specimens prepared from the AF alloy. The [011]β SADP(inset) clearly exhibits additional reflections arising from the ω phase at 1/3 and 2/3 {112}β positions. These ω reflections are an outcome of the orientation relationship between the ω (space group: P6/mmm) and β (space group: Im-3 m) phases: [11–20]ω || [011]β and [0001]ω || [111]β [1]. Fig. 2(b) shows the raw Al and V ion maps from an APT reconstruction from the AF sample, clearly showing nanometer scale pockets depleted in both these elements. These V and Al depleted pockets are indicative of isothermal ω precipitates, since while the α phase rejects V and is enriched in Al, the ω phase rejects out both Al and V. The 8 at%V- isosurface was constructed in the APT reconstruction to more clearly delineate the ω precipitates. A proximity histogram (or proxigram) analysis was carried out to quantify elemental partitioning across ω/β interfaces. The proxigram, shown in Fig. 2(d), revealed that these ω precipitates are depleted in V, Fe, and Al. The V content within ω precipitates is ~4 at%, while the surrounding β matrix is enriched, ~12 at% or 13.5 wt%.

Fig. 3 also shows another region within the same TEM sample and another APT reconstruction from the AF Ti-10–2–3 sample. The dark-field TEM in Fig. 3(a) shows the presence of very fine scale α precipitates within this sample. This is also confirmed by the presence of reflections at ½ {211}β position in the [113]β SADP (inset). While ω reflections are also present in the SADP, the dark-field TEM was recorded using only the α reflection. In contrast, a higher magnification dark-field TEM images encompassing all the reflections (ω at 1/3 and 2/3 {211}β and α at ½{211]β) is shown in Fig. 3(b). The inset shows the same [113]β SADP as shown in Fig. 3(a). The ω particles are about 2–5 nm and exhibit a near-spherical morphology, while the α precipitates exhibit a lath or plate-like morphology with the long axis being ~40–50 nm. APT ion maps in Fig. 3(c) show both the ω and α precipitates. While the Al and V depleted pockets correspond to ω precipitates, the α lath is enriched in Al while being depleted in V, as marked in the Fig. 3(c). A 4.45 at%V- isosurface further allowed quantifying the elemental partitioning across the α/β interface based on a proximity histogram (or proxigram) analysis. The calculated proxigram, shown in Fig. 3(d), indicated that the α precipitate is depleted of Fe and V while being enriched in Al. The α precipitates are depleted in V (~1 at % V), while the surrounding β-matrix is V-rich with ~10 at%. These results establish that the ω precipitates in the AF condition of the Ti-10–2–3 alloy are no longer quenched-in or athermal ω precipitates, i.e., inheriting the composition of the parent β matrix (congruent with the β matrix). Rather, these are isothermal ω precipitates exhibiting a rejection of V, Fe, and Al. This change in the composition of ω precipitates leads to corresponding change in the composition of the β matrix, especially leading to an increase in the V content, consequently increasing the β-phase stability of the matrix. These effects are bound to influence the deformation mechanisms and mechanical properties in this sample, and will be discussed in more detail in subsequent sections

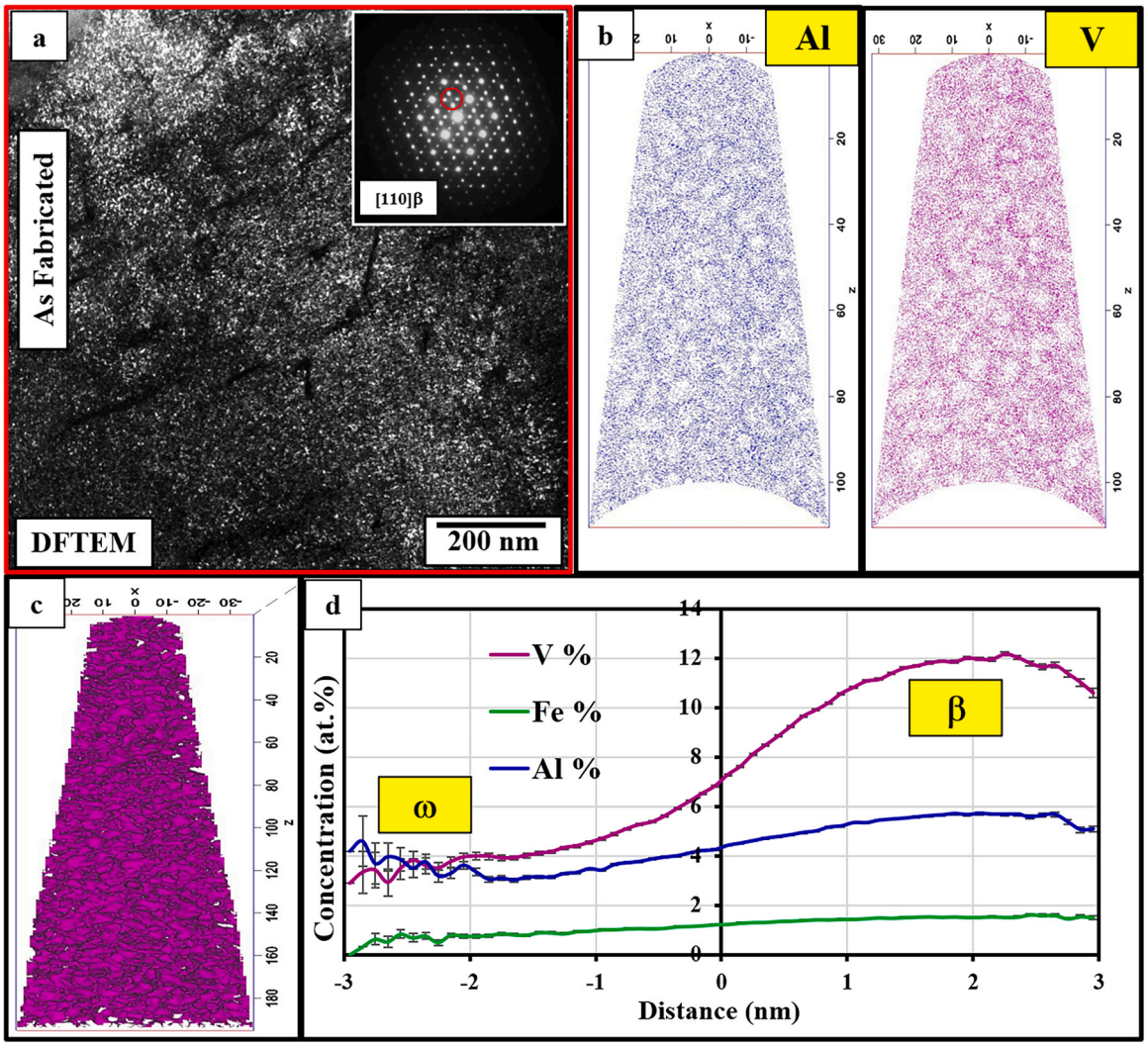

Fig. 2. As-fabricated sample (a) DFTEM showing ω precipitates, inset shows the [011]β SADP from which DFTEM was obtained, (b) raw ion maps of Al and V showing pockets of ω precipitates, (c) V-isosurface and the proximity histogram (d) showing the compositional changes between ω/β phases.

[6–8,15]. Additionally, it should be noted that rejection of solute elements (V, Fe, Al) from the isothermal ω precipitates, most likely occurs during the multiple reheating cycles during the AM processing [40]. Therefore, the AF sample was compared with a β-solutioned condition of the same sample, i.e., the as-fabricated sample annealed at 900 °C for 30 min followed by water quenching. This condition will be henceforth referred to as β-soln. This heat-treatment is also expected to alleviate the residual stresses in the system, arising from AM processing, as well as could potentially recrystallize the β grains in the microstructure [41].

The overall bulk composition obtained from APT analysis is shown in Table 1.

3.2. *Microstructure and mechanical behavior of β-solutionized Ti-10–2-3 alloy*

Similar to the AF condition, following the β-solutionizing, the in-plane microstructure of the sample was investigated. β-solutionizing of the as-fabricated alloy resulted in a significant change in the grain structure as observed in the EBSD IPF map shown in Fig. 4(a). Along with an overall increase in the grain size, to ~350 μm, there is also a notable change in their morphology. The solutionizing treatment also worked in terms of relieving the residual stresses present in the as-fabricated condition, as can be seen in the KAM map in Fig. 4(b). The [011]β SADP, shown in the inset, and the corresponding dark-field TEM image clearly reveal the presence of ω precipitates even after the β-solutionizing heat-treatment (Fig. 4(c)). These observations are consistent with results reported in the literature on conventionally processed Ti-10–2–3 alloy [12,42]. Following the β-solutionizing, tensile testing was carried out on these samples. Similar to the case of the AF condition, three samples of the β-solutionized condition were tensile tested and the engineering stress-strain plot showing the values closest to the average are shown in Fig. 5(a).

In contrast to the AF sample, the β-soln sample exhibits an excellent combination of strength, strain-hardenability, and ductility, especially for an AM processed β-Ti alloy. With YS ~500 MPa and UTS ~1 GPa, the difference between UTS and YS is quite significant (~500 MPa), with a 6% tensile strain-to-failure. Fig. 5(b) puts in context the high strain-hardening (difference between UTS and YS) achieved in this alloy, compared to the other Ti alloys processed via AM. As evident from this plot, the strain-hardening is more than double the nearest alloy. Ti-6Al-4V which is the most commonly used alloy for AM, shows a maximum strain-hardening of ~175 MPa, compared to ~500 MPa observed in the present case. The inset in Fig. 5(a) shows the true stress – true strain tensile curve, and the corresponding work-hardening rate has a value of ~15000 MPa. While previous reports have talked about a high rate of work hardening in other β-Ti alloys [43], the values reported here are higher in comparison. Interestingly, the work-hardening plot also exhibits clear humps as a function of true strain. These humps have been

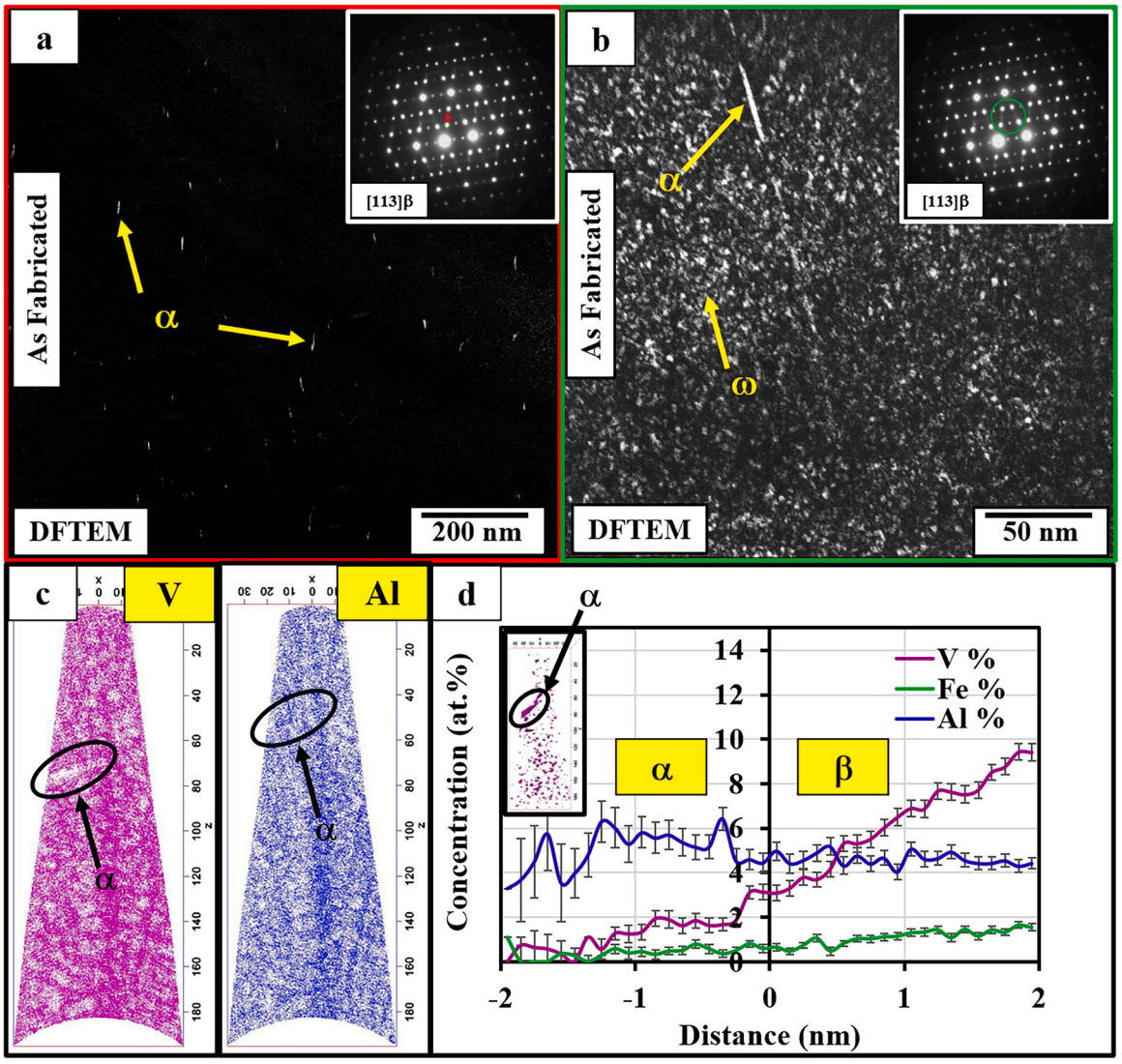

Fig. 3. As-fabricated sample (a) DFTEM showing fine scale α precipitates, inset shows the [113]β SADP from which DFTEM was obtained, (b) DFTEM showing both ω precipitates and fine scale α precipitates, inset shows the [113]β SADP from which DFTEM was obtained, (c) raw ion maps of V and Al showing ω and α precipitates (d) V-isosurface and proximity histogram showing the compositional changes between α/β phases.

Table 1
Composition of the As-fabricated alloy from atom probe tomography.

Element	Ti	V	Fe	Al	O
at%	83.2	8.87	1.33	4.75	.63
wt%	85.7	9.72	1.6	2.76	.22

previously attributed to the TRIP/TWIP effect in β-Ti alloys [10,44] and therefore warrant further investigation. Preliminary SEM imaging, Fig. 5 (c), of the deformed surface clearly shows the presence of stress induced martensite (SIM (α")). It is interesting to note that the formation of α" occurs across multiple length scales. Within the primary network of α" plates, secondary α" plates are also seen, and these have been highlighted in Fig. 5(c) [45–47]. Fig. 5(d) shows the XRD of both conditions, before and after deformation. Prior to deformation, both AF and β-soln conditions exhibited peaks from only single β phase. Post deformation, while there were no additional peaks observed for the AF sample, additional reflections, indicating the presence of the α" phase are evident in the β-soln condition. The presence of additional peaks of α" (112), α" (022) and α" (114) are marked in this XRD pattern. In order to understand the high value of strain-hardening observed in this condition, SEM-EBSD and TEM studies have been further carried out to investigate the deformation behavior of the β-soln sample.

Fig. 6 shows the EBSD analysis, post deformation, of the β-soln sample. Fig. 6(a) shows the schematic of the tensile sample and the locations selected for EBSD analysis. The IPF and phase maps from these locations are shown in the series, Fig. 6(b–e). A significant change in the overall phase fraction of α" is observed in these different regions. This is possibly due to the orientation of the grains and the consequently the Schmid factor. Similar observations have been previously reported by Lilensten et al. [48]. Multiple intersections of α" laths can be observed in the IPF images (marked with arrows) and at these intersections, significant shear displacements are visible, which are indicative of strain localization as discussed in previous reports [21]. Based off of these analyses two regions were further investigated in further detail coupling EBSD at higher magnification and TEM analysis; (i) region which had 36% α" and (ii) region which has 93% α".

The EBSD IPF+IQ map and discrete pole figures in Fig. 7 leads to more insights into the deformation behavior. Area of interest 1, shown in Fig. 7(a), shows the intersection of two stress induced martensite laths. The discrete plots confirm the existence of the standard OR between β and α", i.e. {110}β // (001)α" [45]. It is also interesting to note that two distinct α" laths also have the standard twin relation of {111}α" as can

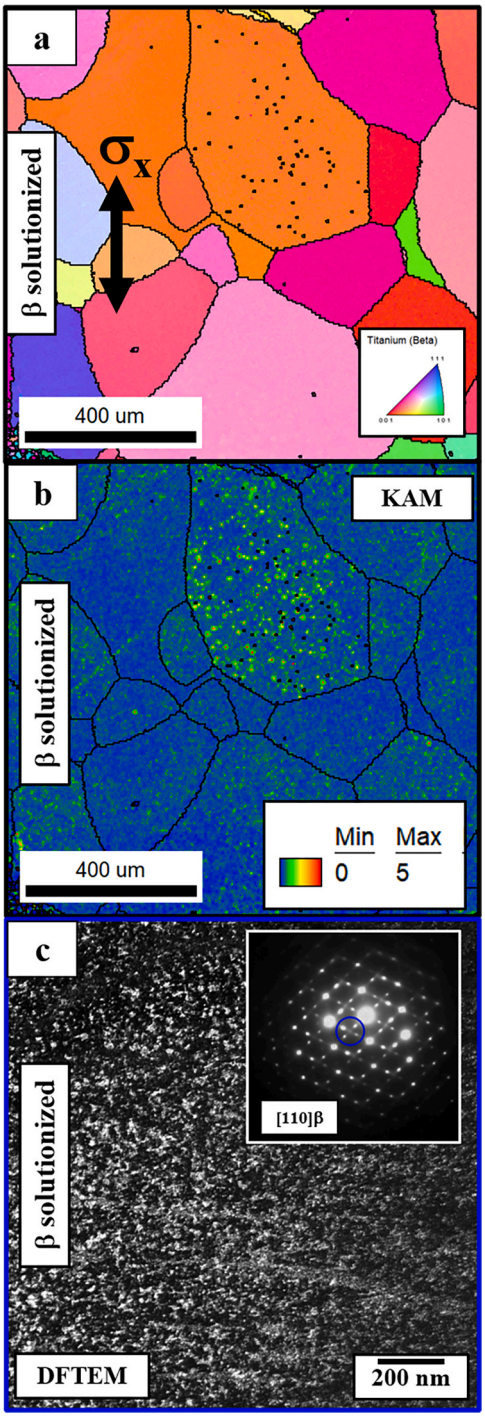

Fig. 4. Starting microstructure of the β-solutionized sample, (a) EBSD IPF map, (b) KAM map, (c) DFTEM image showing ωathermal and the SADP from where the DFTEM were captured.

be seen in the discrete plot labeled 3. Area of interest 2 shows the presence of twins inside the martensite lath. These are most probably transformation twins formed during the formation of stress induced martensite laths [44,49] also share a {111}α" plane. These are generally labeled as type I twins [50].

The regions of the retained parent β matrix in this area of the tensile sample, corresponding to 36% of α" and 64% of β (shown in Fig. 6(c)) have been further investigated via site-specific TEM examination. An approximate area from where the FIB lift-out was extracted has been indicated with a box in Fig. 7 and the bright-field TEM image of this TEM sample is shown in Fig. 8(a). Two regions highlighted in this area have been further investigated and corresponding magnified images are shown in Fig. 8(b) (Region 1) and 8(e) (Region 2) respectively. Region 1 shows the presence of a band, on which further conventional diffraction and precession electron diffraction (PED) analysis was carried out. The PED data shown in Fig. 8(d) shows the IQ + IPF, and IQ + phase map. The phase map clearly indicates the presence of the α" phase within the β matrix. Even at this scale, multiple intersections of these α" laths can be noted. The diffraction patterns from the three different locations marked in Fig. 8(d) are shown below. These were obtained using the Acom software after the data collection via the Topspin 3.0 software. As can be seen, the three diffraction patterns show the orientation relationship between the β matrix and α" laths, i.e. [113]β || [112]α". This was also confirmed by the conventional TEM selected area diffraction pattern, shown in Fig. 7(c), recorded along the [113]β ZA. The additional spots in this diffraction pattern also confirm the presence of α". The retained β regions, highlighted by the orange box (Region 2), also exhibit interesting features, especially with respect to the ω precipitates. The shearing of these precipitates influences the deformation behavior and mechanical properties of this β-soln sample, as compared to the as-fabricated sample.

The discrete pole figures corresponding to the different α" variants and the adjacent β matrix phase have been plotted in the figure. Similar to sample which had 36% α", the two areas of interest showed different variants of α" laths as well as internal twinning within these martensite laths. With respect to area of interest 1, the expected{001}α"//{011}β orientation relationship between the α" variants and the adjacent β matrix is noted, while also showing twin relation along {111}α" plane. With respect to area of interest 2, Fig. 9(e) shows the pole figures for a thick α" lath and the internal twin present within this lath. These pole figures clearly establish that the that internal twinning is of the {111} type [42,50].

TEM analysis was also carried out on a sample extracted from within the area of interest 2 as shown in Fig. 9(a). As noted earlier, this region is closest to the fracture site, i.e., 93% α". This TEM sample (Fig. 10(a)) predominantly comprised a single thick primary α" lath, which shows internal hierarchical features. Two specific regions have been highlighted in Fig. 10(a). Fig. 10(b) corresponding to highlighted region in red, exhibits an internal twin within the primary α" lath. Furthermore, within this primary twin, there are finer scale secondary twins as shown in Fig. 10(b). The corresponding selected area diffraction pattern from the lath, encompassing the twins, is shown in Fig. 10(c) and confirms the primary twin orientation with additional spots corresponding to the internal secondary twinning. Interestingly, in the magnified view of the highlighted region in green, shown in Fig. 10(e), a small patch of the parent β-matrix along with stress induced martensite laths was noted. The DFTEM images shown in Fig. 10 (e) and (f) are taken from the spots highlighted in Fig. 10 (d). The high strain-hardening observed in the AM fabricated plus β-soln Ti-10–2–3 alloy can be attributed to this hierarchical microstructure containing stress-induced martensite laths of different size scales coupled with hierarchical internal twinning within these α" laths [31,41].

APT studies were also performed on the β-solutionized sample. The raw ion maps shown in Fig. 11 (a–c) do not exhibit any discernible pockets devoid or enriched in any of the solute atoms. Additionally, frequency distribution analysis was performed on the raw data of the V ions and compared to a theoretical binomial distribution (representing a random distribution). The concentration of V was calculated in every 100 ion bins, and the V-rich section of the histogram frequency vs. V concentration is plotted in Fig. 11(d). Additionally, the binomial distribution has also been shown in the same plot and both the distributions are almost identical. Therefore, APT could not detect composition partitioning in the β-solutionized condition. However, as shown in Fig. 4(c), this microstructure consists of a very high number density of fine scale ω precipitates within the β matrix, and the APT results establish that these quenched-in precipitates are athermal ω precipitates which inherit the

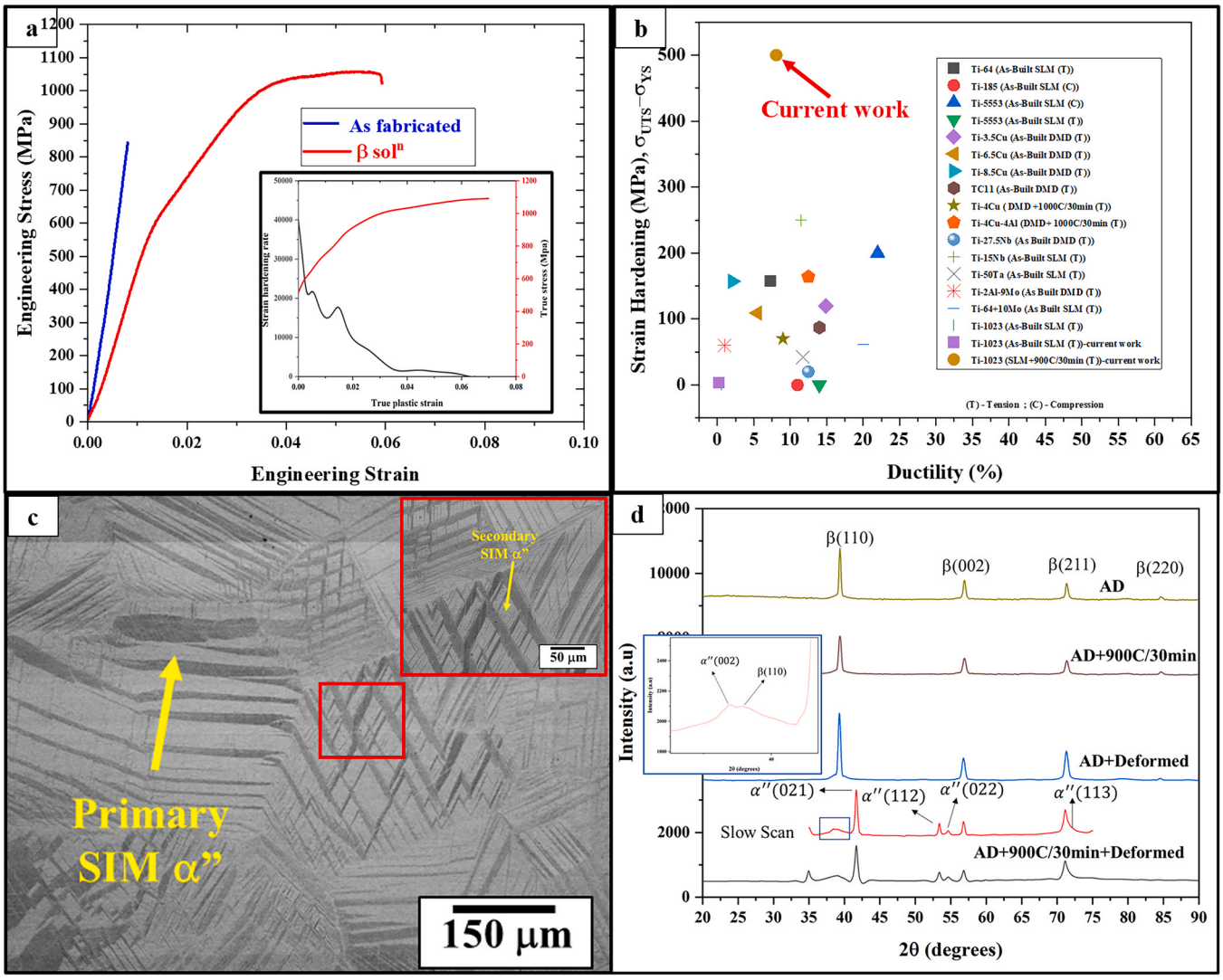

Fig. 5. (a) Engineering stress-strain curves of the β-soln conditions. Inset shows the true stress v true strain curve along with the corresponding strain-hardening rates of the β-soln sample, (b) Ashby plot comparing the strain hardening of the current alloy with other AM processed Ti-alloys, (c) SEM micrographs of the deformed surface showing SIM (α”) across multiple length scales (d) XRD of the two conditions before and after deformation. Additional peaks of α” were noted in the β-soln condition post deformation.

composition of the parent β matrix.

3.3. Comparison of the microstructure and mechanical behavior of as-fabricated and β-solutionized Ti-10–2-3 alloy

The experimental observations indicate a substantial difference between the deformation behaviors of the AF and β-soln conditions of the AM processed Ti-10–2–3 alloy, with exceptional strain hardening resulting from stress-induced martensite formation or TRIP effect in case of the latter condition. Possible reasons underlying this difference, based on previous reports in the literature, include differences in the grain size and morphology [51–55], and the chemical composition of the parent β matrix [7,25,26]. Previous reports on the Ti-10–2–3 and other metastable β-alloys, emphasize the effect of grain size on the triggering stress required for stress-induced martensite formation. This triggering stress has been reported to initially decrease with an increase in grain size, reaching a minimum value, and subsequently again increase with a further increase in grain size [54]. Comparing the AF and β-soln conditions in the present case, while the grain size increases from ~100 μm to ~350 μm, these grain sizes are too large to exhibit any significant difference in the triggering stress for the TRIP effect. The chemical composition of the β-phase is another important factor in determining the degree of metastability of the β phase and consequently the deformation behavior of β-Ti alloys [6,7]. With an increase in the β phase stability, the deformation behavior changes from TRIP to TWIP, and finally to dislocation slip. A previously reported investigation has shown that in case in a binary Ti-12Mo alloy, a change in the chemical composition of the parent β-matrix phase, due to Mo partitioning between the matrix and isothermal ω precipitates, leads to a change in the deformation behavior from TRIP/TWIP to slip [7,13,56]. Similar observations were also made by Lai et al. in their work on Ti–25 Nb–0.7Ta–2Zr (at%) alloy [6]. The SLM processed AF Ti-10–2–3 alloy, in the present study, undergoes multiple heating-cooling cycles during AM processing, which could potentially lead to a change in the chemical composition of the β matrix due to partitioning of alloying elements between β and ω, thus causing the sample to deform via slip, and not via TRIP/TWIP.

The APT results indicate that while the β phase in case of the AF sample contains ~12 at% V, after β-solutionizing the alloy contains ~9.3 at% V. While this is a measurable difference in the chemical composition of the β-matrix, it is not sufficiently large to be solely responsible for changing the deformation behavior, unlike the previous

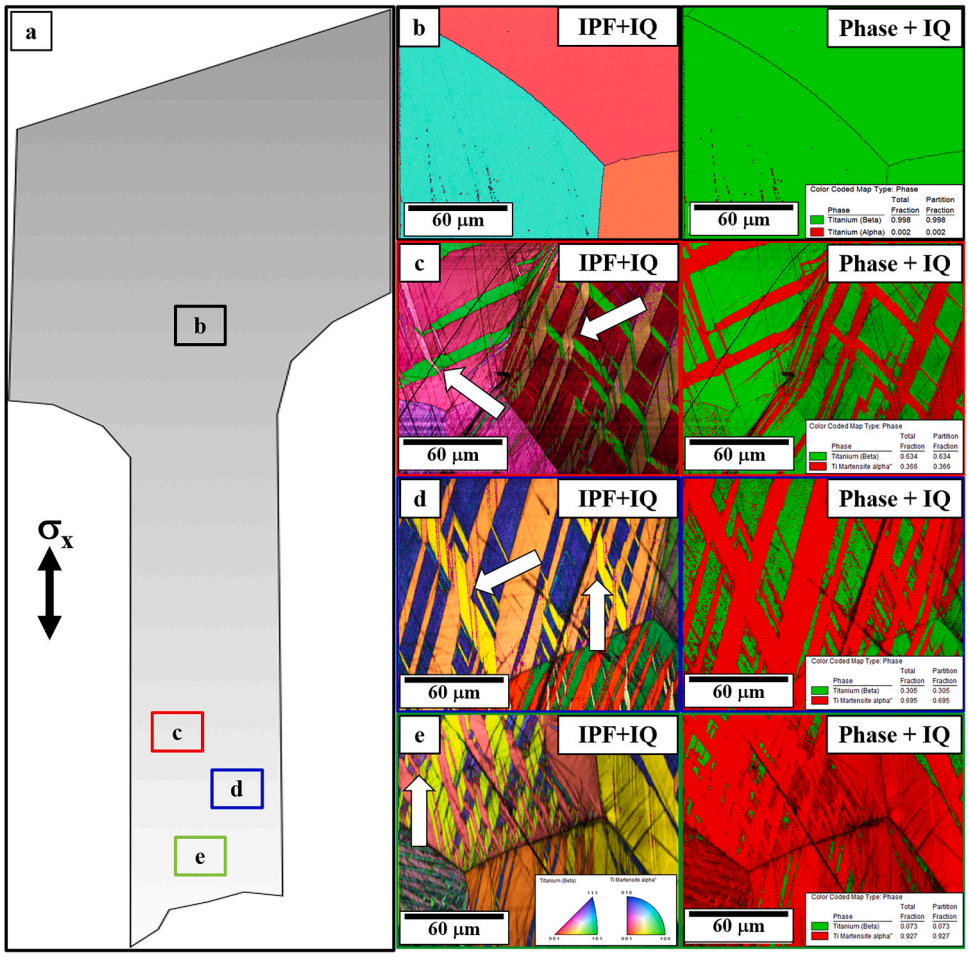

Fig. 6. (a) Schematic of the tensile sample post fracture, and corresponding EBSD maps ((b), (c), (d), (e)) from the different locations indicated on the schematic.

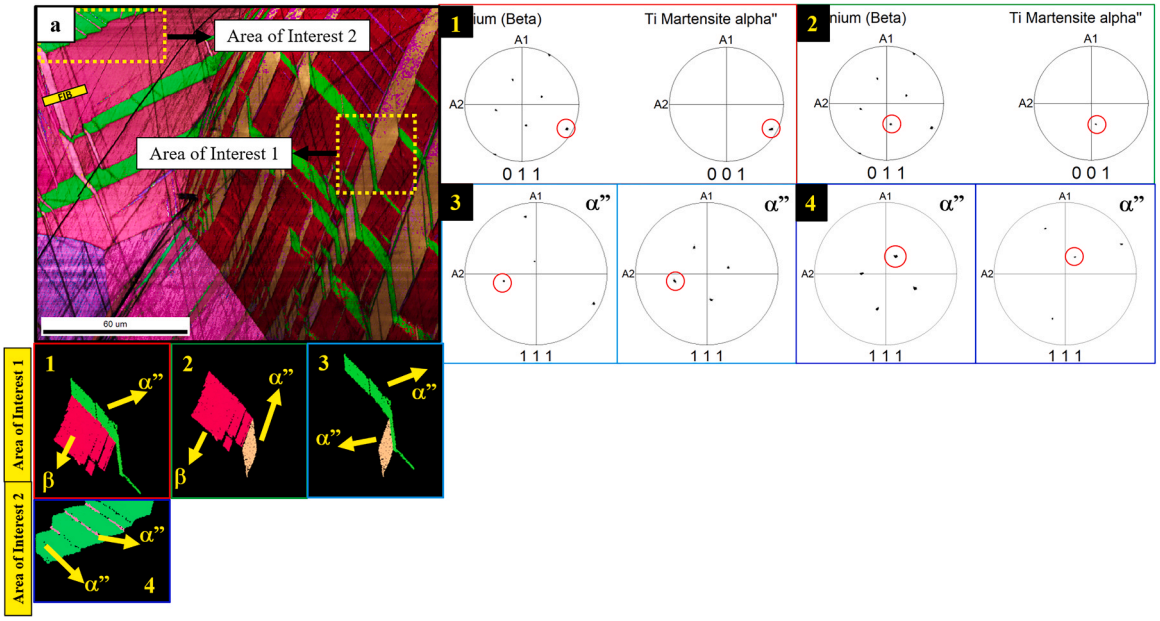

Fig. 7. EBSD IPF+IQ maps of sample which had 37% α" showing two areas of interest and their corresponding discrete plots identifying orientation relationships.

report on the Ti-12Mo alloy [7]. Therefore, the role of the ω precipitates on the deformation behavior and mechanical properties needs to be considered. Based off of the APT results (AF and β-soln), while the isothermal ω precipitates contain ~4 at% V in case of the AF condition, the athermal ω precipitates contain ~9.3 at% V in case of the β-soln condition.

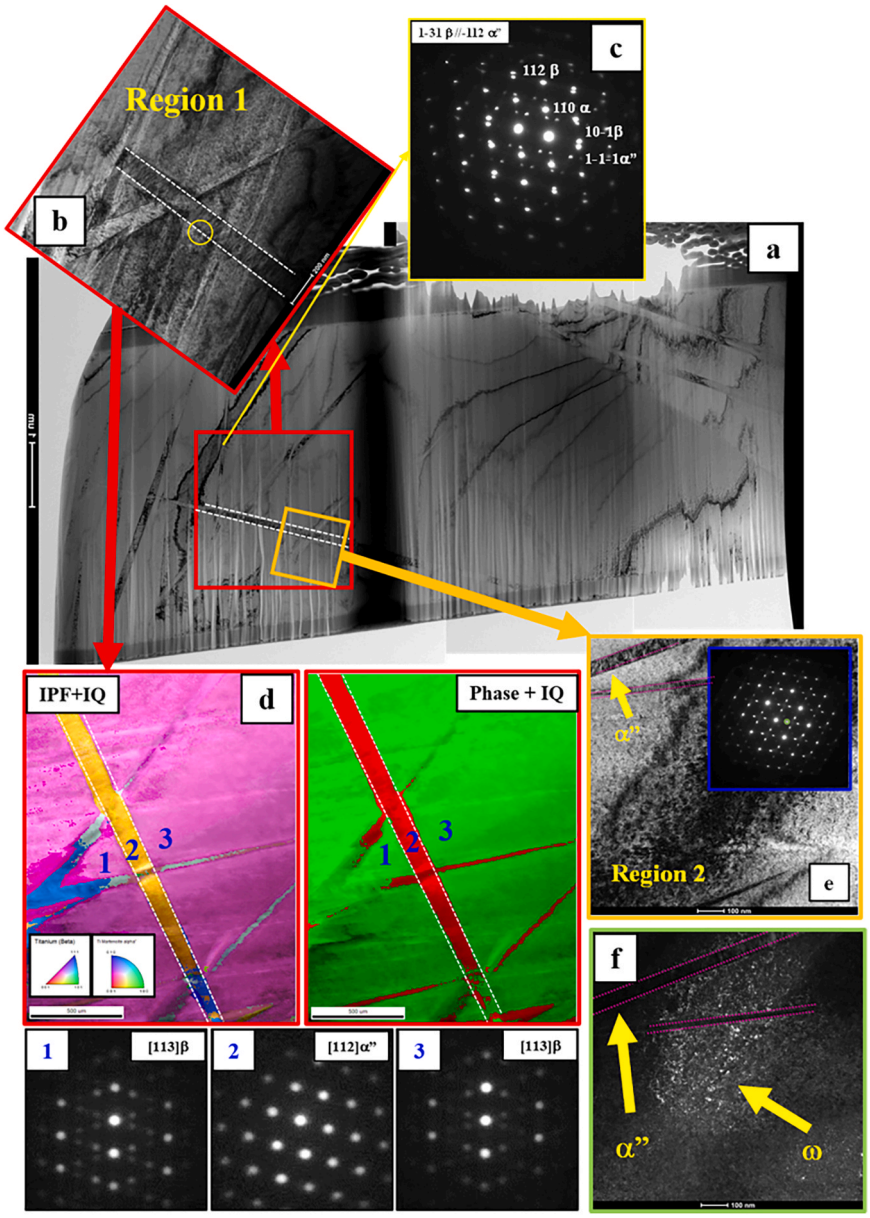

Fig. 8. TEM analysis of the site-specific sample from region which had 37% α" in Fig. 6.

3.4. Role of athermal versus isothermal ω precipitates on deformation behavior of Ti-10-2-3

There has been a substantial amount of discussion in the literature on the role of ω phase precipitates on the plasticity, deformation behavior, and tensile properties of titanium alloys. It has been well-established in many previous reports that athermal or quenched-in ω precipitates, which inherit the composition of the parent β matrix, are typically not detrimental to plastic behavior. Therefore, titanium alloys with such athermal ω precipitates are often quite ductile and exhibit good strain-hardenability [13,15,56]. Contrastingly, it has been reported that in cases where there is a compositional partitioning between the β and ω phases, referred to as isothermal ω precipitates, there is often an increase in yield strength, accompanied by a severe loss of ductility [6,7,57,58]. Despite these previously reported experimental observations, the underlying mechanism leading to such increase in yield strength, but accompanied with loss of ductility, is not well understood. Lai et al. in a recent study on Ti-Nb-Zr-Ta alloys, indicates the role of Nb content on the shear modulus of ω precipitates, and subsequently the deformation behavior of the alloy [6]. We noticed a similar effect in the current system, wherein the densely distributed ω particles in the AF condition act as barriers for the transformation induced plasticity effect by suppressing the martensite formation. A combination of that and the formation of the ω precipitates and some fine scale α precipitates due to the multiple reheating cycles, leads to an enrichment of the β-stabilizers in the parent β-matrix, subsequently causing the sample to deform via slip.

4. Summary

Summarizing, this paper reports reactivation of transformation induced plasticity (TRIP) in an AM (laser powder bed fusion) processed commercial β-Ti alloy, Ti-10V-2Fe-3Al (wt%). While the as-fabricated alloy exhibited a high yield strength (~950 MPa), it had virtually no strain hardenability and tensile ductility. Interestingly, after this as-fabricated alloy was subjected to a β-solutionizing treatment, it exhibited substantial recovery of tensile ductility coupled with very high strain hardening (tensile strength minus yield strength ~500 MPa), and a significantly high strain hardening rate ~15000. The extraordinarily

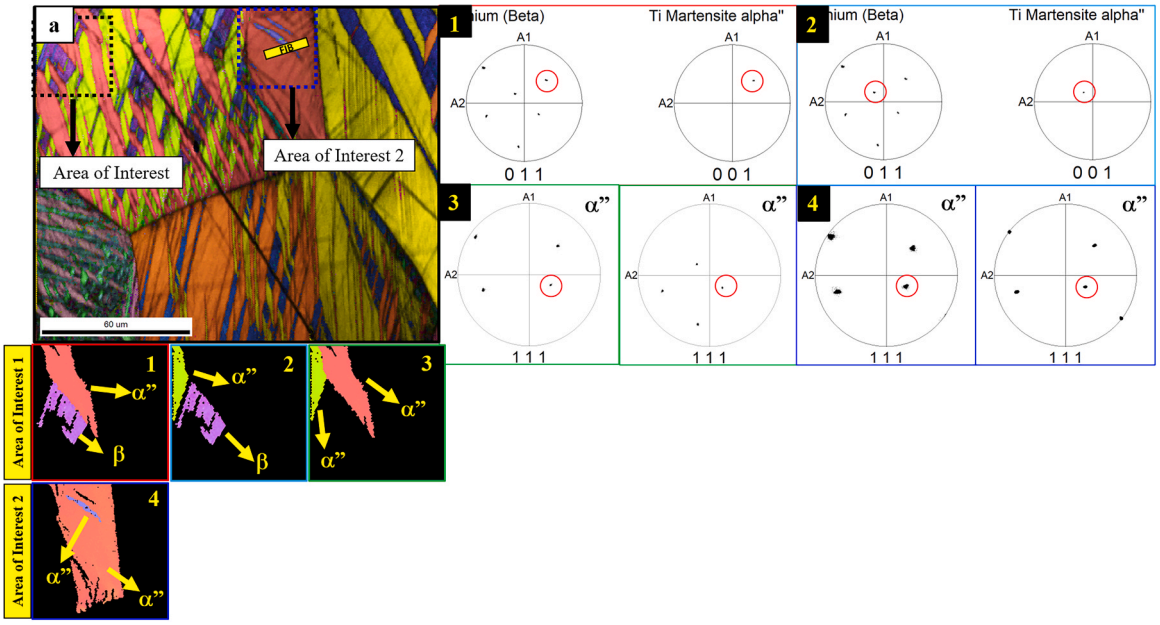

Fig. 9. EBSD IPF+IQ maps of sample which had 93% α” showing two areas of interest and their corresponding discrete plots identifying orientation relationships.

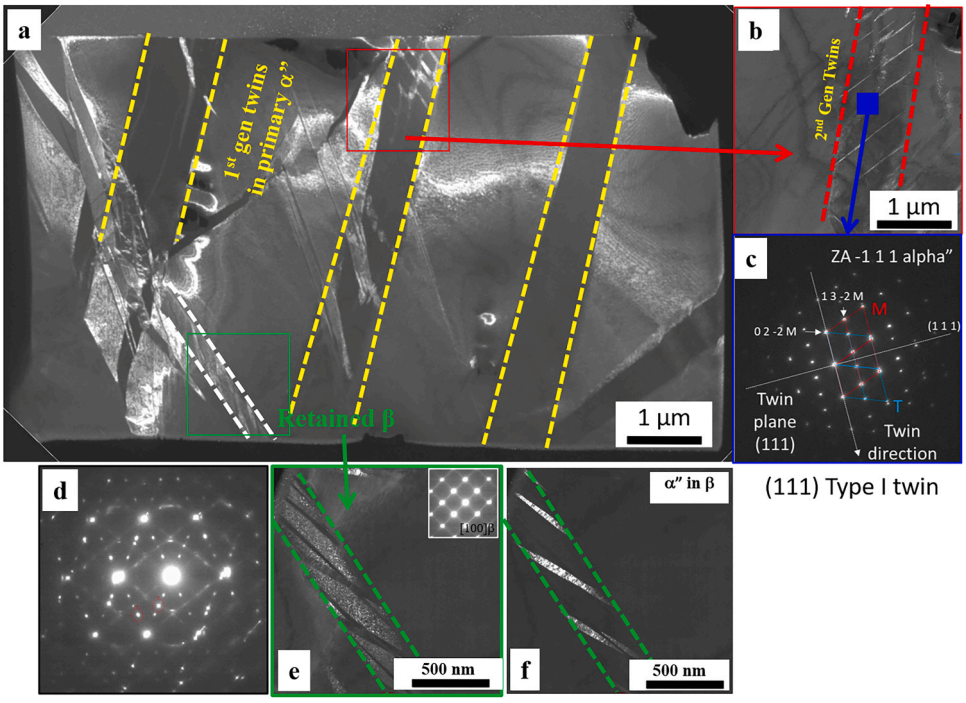

Fig. 10. TEM analysis of the site-specific sample from region which had 93% α” in Fig. 6. Hierarchical features including first and second generations twins formed within the stress induced martensite lath can be seen.

high strain hardening rate in AM processed and β-solutionized Ti-10–2–3 alloy can be attributed to relatively thick stress-induced martensitic α” laths/plates, exhibiting a hierarchical internally twinned microstructure, comprising multiple generations of deformation induced twins. The recovery of the TRIP effect in this alloy after the β-solutionizing treatment can be attributed to the reversal from hard non-shearable isothermal ω precipitates in the as AM processed condition, to softer shearable athermal ω precipitates in the β-solutionized condition. Exploiting the TRIP effect in AM processed Ti alloys can potentially lead to substantially higher tensile strengths and uniform ductility in this critical class of lightweight high strength engineering alloys.

CRediT authorship contribution statement

S A Mantri: Conceptualization, Formal analysis, Investigation, Writing – original draft. **M S K K Y Nartu:** Formal analysis, Investigation, Writing – review & editing. **S Dasari:** Formal analysis, Investigation, Writing – review & editing. **A Sharma:** Formal analysis, Investigation. **P Agrawal:** Formal analysis, Investigation. **R Salloom:** Formal analysis, Investigation. **F Sun:** Formal analysis, Investigation, Writing – review & editing. **K. Cho:** Funding acquisition, Supervision. **B**

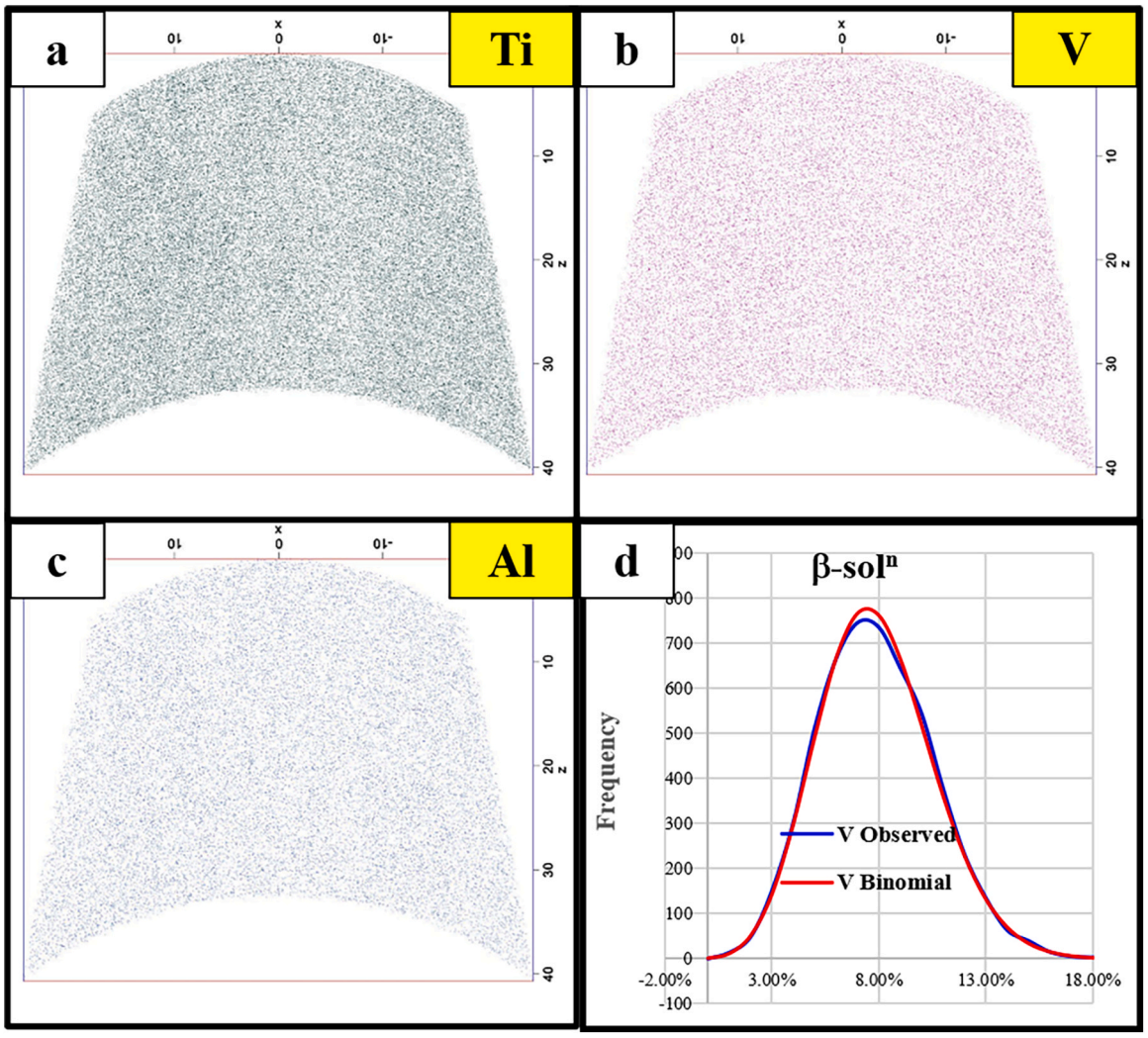

Fig. 11. APT of β-soln sample, raw ion maps of (a) Ti, (b) V, and (c) Al does not show any partitioning, which is further corroborated by LBM plot (d).

McWilliams: Funding acquisition, Supervision. **E Ivanov:** Resources. **S. G. Srinivasan:** Funding acquisition, Resources, Supervision, Writing – review & editing. **N.B. Dahotre:** Funding acquisition. **F Prima:** Supervision, Writing – review & editing. **R. Banerjee:** Conceptualization, Funding acquisition, Resources, Supervision, Writing – review & editing.

Declaration of Competing Interest

The authors declare that they have no known competing financial interests or personal relationships that could have appeared to influence the work reported in this paper.

Acknowledgements

This research has been supported in part by the National Science Foundation (NSF), Division of Materials Research (DMR) under grant DMR-1905844. The authors also acknowledge financial support for this work from a cooperative agreement between the U.S. Army Research Laboratory (ARL) and the University of North Texas; W911NF-19-2-0011. We also acknowledge the infrastructure and support of Center for Agile & Adaptive and Additive Manufacturing (CAAAM) funded through State of Texas Appropriation #190405-105-805008-220 at the University of North Texas. AFOSR grant FA9550-20-1-0169 is also acknowledged.

References

[1] D. Banerjee, J. Williams, Perspectives on titanium science and technology, Acta Mater. 3 (2013) 844–879.
[2] G. Welsch, R. Boyer, E. Collings, Materials Properties Handbook: Titanium Alloys, ASM, 1993.
[3] J. Cotton, R. Briggs, R. Boyer, S. Tamirisakandala, P. Russo, N. Shchetnikov, J. Fanning, State of the art in beta titanium alloys for airframe applications, JOM 67 (6) (2015) 1281–1303.
[4] O. Ivasishin, P. Markovsky, Y. Matviychuk, S.W.C. Semiatin, S. Fox, A comparative study of the mechanical properties of high-strength β-titanium alloys, J. Alloy. Compd. 457 (1–2) (2008) 296–309.
[5] F. Sun, J. Zhang, M. Marteleur, T. Gloriant, P. Vermaut, D. Laille, P. Castany, C. Curfs, P. Jacques, F. Prima, Investigation of early stage deformation mechanisms in a metastable β titanium alloy showing combined twinning-induced plasticity and transformation-induced plasticity effects, Acta Mater. 61 (17) (2013) 6406–6417.
[6] M. Lai, T. Li, D. Raabe, ω phase acts as a switch between dislocation channeling and joint twinning- and transformation-induced plasticity in a metastable β titanium alloy, Acta Mater. 151 (2018) 67–77.
[7] S. Mantri, D. Choudhuri, T. Alam, V. Ageh, F. Sun, F. Prima, R. Banerjee, Change in the deformation mode resulting from beta-omega compositional partitioning in a TiMo alloy: room versus elevated temperature, Scr. Mater. 130 (2015) 69–73.
[8] W. Wang, X. Zhang, J. Sun, Phase stability and tensile behavior of metastable β Ti-V-Fe and Ti-V-Fe-Al alloys, Mater. Charact. 142 (2018) 398–405.
[9] Q. Sun, S. Song, R. Zhu, H. Gu, Toughening of titanium alloys by twinning and martensite transformation, J. Mater. Sci. 37 (2002) 2543–2547.
[10] J. Gao, Y. Huang, D. Guan, A. Knowles, L. Ma, D. Dye, W. Rainforth, Deformation mechanisms in a metastable beta titanium twinning induced plasticity alloy with high yield strength and high strain hardening rate, Acta Mater. 152 (2018) 301–314.
[11] N. Chen, H. Kou, Z. Wu, F. Qiang, C. Wang, J. Li, J. Molina-Aldareguia, Stress-induced α″ martensitic phase transformation and martensitic twinning in a metastable β titanium alloy, J. Alloy. Compd. 859 (2020), 157809.

[12] T. Duerig, G. Terlinde, J. Williams, Phase transformations and tensile properties of Ti-^{10}V–^{2}Fe-3AI, Metall. Trans. A 11 (12) (1980) 1987–1998.
[13] F. Sun, J. Zhang, P. Vermaut, D. Choudhuri, T. Alam, S. Mantri, P. Svec, T. Gloriant, P. Jacques, R. Banerjee, F. Prima, Strengthening strategy for a ductile metastable β-titanium alloy using low-temperature aging, Mater. Res. Lett. 5 (8) (2017) 547–553.
[14] S. Mantri, D. Choudhuri, T. Alam, G. Viswanathan, J. Sosa, H. Fraser, R. Banerjee, Tuning the scale of α precipitates in β-titanium alloys for achieving high strength, Scr. Mater. 154 (2018) 139–144.
[15] M. Lai, T. Li, F. Yan, J. Li, D. Raabe, Revisiting ω phase embrittlement in metastable β titanium alloys: role of elemental partitioning, Scr. Mater. 193 (2021) 38–42.
[16] K. P.A, S. Semiatin, The laser additive manufacture of Ti-6Al-4V, JOM 53 (2001) 40–42.
[17] L. Thijs, F. Verhaeghe, T. Craeghs, J. Humbeeck, J.-P. Kruth, A study of the microstructural evolution during selective laser melting of Ti–6Al–4V, Acta Mater. 58 (9) (2010) 3303–3312.
[18] M. Simonelli, Y. Tse, C. Tuck, Effect of the build orientation on the mechanical properties and fracture modes of SLM Ti–6Al–4V, Mater. Sci. Eng. A 616 (2014) 1–11.
[19] H. Schwab, F. Palm, U. Kuhn, J. Eckert, Microstructure and mechanical properties of the near-beta titanium alloy Ti-5553 processed by selective laser melting, Mater. Des. 105 (2016) 75–80.
[20] M. Bermingham, D. Kent, B. Pace, J. Cairney, M. Dargusch, High strength heat-treatable β-titanium alloy for additive manufacturing, Mater. Sci. Eng. A 791 (2020), 139646.
[21] W. Sames, F. List, S. Pannala, R. Dehoff, S. Babu, The metallurgy and processing science of metal additive manufacturing, Int. Mater. Rev. 61 (5) (2016) 315–360.
[22] T. DebRoy, H. Wei, J. Zuback, T. Mukherjee, J. Elmer, J. Milweski, A. Beese, A. Wilson-Heid, A. De, W. Zhang, Additive manufacturing of metallic components – process, structure and properties, Prog. Mater. Sci. 92 (2018) 112–224.
[23] G. Lutjering, J. Williams, Titanium, Springer, 2007.
[24] H. Azizi, H. Zurob, B. Bose, R. Ghiaasiaan, X. Wang, S. Coulson, V. Duz, A. Phillion, Additive manufacturing of a novel Ti-Al-V-Fe alloy using selective laser melting, Addit. Manuf. 21 (2018) 529–535.
[25] D. Zhang, D. Qiu, M. Gibson, Y. Zheng, H. Fraser, D. John St, M. Easton, Additive manufacturing of ultrafine-grained high-strength titanium alloys, Nature 576 (2019) 91–95.
[26] S. Mantri, T. Alam, Y. Zheng, J. Williams, R. Banerjee, Influence of post deposition annealing on microstructure and properties of laser additively manufactured titanium copper alloys, Addit. Manuf. 32 (2020), 101067.
[27] Q. Liu, C. Qiu, Variant selection of α precipitation in a beta titanium alloy during selective laser melting and its influence on mechanical properties, Mater. Sci. Eng. A 784 (2020), 139336.
[28] T. Duerig, J. Albrecht, D. Richter, P. Fischer, Formation and reversion of stress induced martensite in Ti-10V–2Fe-3Al, Acta Metall. 30 (12) (1982) 2161–2172.
[29] S. Neelakantan, D. San Martin, P. Rivera-Diaz-del-Castillo, S. van der Zwaag, Plasticity induced transformation in a metastable β Ti-1023 alloy by controlled heat treatments, Mater. Sci. Technol. 25 (11) (2009) 1351–1358.
[30] A. Bhattacharjee, S. Bhargava, V.K.S. Varma, A. Gogia, Effect of β grain size on stress induced martensitic transformation in β solution treated Ti–10V–2Fe–3Al alloy, Scr. Mater. 53 (2) (2005) 195–200.
[31] T. Akanuma, H. Matsumoto, S. Sato, A. Chiba, I. Inagaki, Y. Shirai, T. Maeda, Enhancement of athermal α″ martensitic transformation in Ti–10V–2Fe–3Al alloy due to high-speed hot deformation, Scr. Mater. 67 (1) (2012) 21–24.
[32] L. Qi, X. Qiao, L. Huang, X. Huang, X. Zhao, Effect of structural stability on the stress induced martensitic transformation in Ti-10V–2Fe-3Al alloy, Mater. Sci. Eng. A 756 (2019) 381–388.
[33] Y. Danard, R. Poulain, M. Garcia, R. Guillou, D. Thiaudiere, S. Mantri, R. Banerjee, F. Sun, F. Prima, Microstructure Design and in-situ investigation of TRIP/TWIP effects in a forged dual-phase Ti–10V–2Fe–3Al alloy, Materialia 8 (2019), 100507.
[34] C. Qiu, Q. Liu, Multi-scale microstructural development and mechanical properties of a selectively laser melted beta titanium alloy, Addit. Manuf. 30 (2019), 100893.
[35] M. Komarasamy, Deformation Micro-mechanisms of Simple and Complex Concentrated FCC Alloys: Dissertation Prepared for the Degree of Doctor of Philosphy, Denton, 2015.
[36] T. Nagase, T. Hori, M. Todai, S. Sun, T. Nakano, Additive manufacturing of dense components in beta-titanium alloys with crystallographic texture from a mixture of pure metallic element powders, Mater. Des. 173 (2019), 107771.
[37] L. Carter, C. Martin, P. Withers, M. Attallah, The influence of the laser scan strategy on grain structure and cracking behaviour in SLM powder-bed fabricated nickel superalloy, J. Alloy. Compd. 615 (2014) 338–347.
[38] X. Ma, Z. Chen, L. Xiao, W. Lu, S. Luo, Y. Mi, Compressive deformation of a metastable β titanium alloy undergoing a stress-induced martensitic transformation: The role of β grain size, Mater. Sci. Eng. A 794 (2020), 139919.
[39] X. Ma, Z. Chen, L. Xiao, S. Luo, W. Lu, Stress-induced martensitic transformation in a β-solution treated Ti–10V–2Fe–3Al alloy during compressive deformation, Mater. Sci. Eng. A 801 (2021), 140404.
[40] M. Nartu, S. Dasari, A. Sharma, S. Mantri, S. Sharma, M. Pantawane, B. McWilliams, K. Cho, N. Dahotre, R. Banerjee, Omega versus alpha precipitation mediated by process parameters in additively manufactured high strength Ti–1Al–8V–5Fe alloy and its impact on mechanical properties, Mater. Sci. Eng. A 821 (2021), 141627.
[41] C. Li, J. Chen, Y. Ren, W. Li, J. He, J. Chen, Effect of solution heat treatment on the stress-induced martensite transformation in two new titanium alloys, J. Alloy. Compd. 641 (2015) 192–200.
[42] W. Chen, J. Zhang, S. Cao, Y. Pan, M. Huang, Q. Hu, Q. Sun, L. Xiao, J. Sun, Strong deformation anisotropies of ω-precipitates and strengthening mechanisms in Ti-10V–2Fe-3Al alloy micropillars: precipitates shearing vs precipitates disordering, Acta Mater. 68–80 (2016) 117–180.
[43] Y. Fu, W. Xiao, D. Kent, M. Dargusch, J. Wang, X. Zhao, C. Ma, Ultrahigh strain hardening in a transformation-induced plasticity and twinning-induced plasticity titanium alloy, Scr. Mater. 187 (2020) 285–290.
[44] E. Bertrand, P. Castany, Y. Yang, E. Menou, T. Gloriant, Deformation twinning in the full-α″ martensitic Ti–25Ta–20Nb shape memory alloy, Acta Mater. 105 (2016) 94–103.
[45] Y. Yang, P. Castany, Y. Hao, T. Gloriant, Plastic deformation via hierarchical nano-sized martensitic twinning in the metastable β Ti-24Nb-4Zr-8Sn alloy, Acta Mater. 194 (2020) 27–39.
[46] P. Castany, Y. Yang, E. Bertrand, T. Gloriant, Reversion of a parent {130}⟨ 310⟩ α″ martensitic twinning system at the origin of {332}⟨ 113⟩ β twins observed in metastable β titanium alloys, Phys. Rev. Lett. 245501 (2016) 117.
[47] S. Mantri, F. Sun, D. Choudhuri, T. Alam, B. Gwalani, F. Prima, R. Banerjee, Deformation induced hierarchical twinning coupled with omega transformation in a metastable β-Ti alloy, Sci. Rep. 9 (1) (2019) 1–8.
[48] L. Lilensten, Y. Danard, C. Brozek, S. Mantri, P. Castany, T. Gloriant, P. Vermaut, F. Sun, R. Banerjee, F. Prima, On the heterogeneous nature of deformation in a strain-transformable beta metastable Ti-V-Cr-Al alloy, Acta Mater. 162 (2019) 268–276.
[49] Y. Chai, H. Kim, H. Hosoda, S. Miyazaki, Self-accommodation in Ti–Nb shape memory alloys, Acta Mater. 57 (2009) 4054–4064.
[50] X. Ji, I. Gutierrez-Urrutia, S. Emura, T. Liu, T. Hara, X. Min, D. Ping, K. Tsuchiya, Twinning behavior of orthorhombic-α" martensite in a Ti-7.5Mo alloy, Sci. Technol. Adv. Mater. 20 (1) (2019) 401–411.
[51] M.-H. Cai, C.-H. Lee, Y.-K. Lee, Effect of grain size on tensile properties of fine-grained metastable β titanium alloys fabricated by stress-induced martensite and its reverse transformations, Scr. Mater. 66 (8) (2012) 606–609.
[52] Y. Zhu, X. Liao, X. Wu, J. Narayan, Grain size effect on deformation twinning and detwinning, J. Mater. Sci. 48 (2013) 4467–4475.
[53] F. Niessen, A. Gazder, D. Mitchell, E. Pereloma, In-situ observation of nucleation, growth and interaction of deformation-induced α″ martensite in metastable Ti–10V–2Fe–3Al, Mater. Sci. Eng. A (2020), 140237.
[54] A. Paradkar, S. Kamat, A. Gogia, B. Kashyap, Trigger stress for stress-induced martensitic transformation during tensile deformation in Ti-Al-Nb alloys: effect of grain size, Metall. Mater. Trans. A 39 (3) (2008) 551–558.
[55] S. Sadeghpour, S. Abbasi, M. Morakabati, Deformation-induced martensitic transformation in a new metastable β titanium alloy, J. Alloy. Compd. 650 (2015) 22–29.
[56] B. Ellyson, J. Klemm-Toole, K. Clarke, R. Field, M. Kaufman, A. Clarke, Tuning the strength and ductility balance of a TRIP titanium alloy, Scr. Mater. 194 (2021), 113641.
[57] S. Mantri, D. Choudhuri, A. Behera, M. Hendrickson, T. Alam, R. Banerjee, Role of isothermal omega phase precipitation on the mechanical behavior of a Ti-Mo-Al-Nb alloy, Mater. Sci. Eng. A 767 (2019), 138397.
[58] S. Banerjee, U. Naik, Plastic instability in an omega forming Ti-15% Mo alloy, Acta Mater. 44 (9) (1996) 3667–3677.